Exploring Respiratory Motion Tracking through Electrical Impedance Tomography (EIT)

Exploring Respiratory Motion Tracking through Electrical Impedance Tomography (EIT)

Qi Wang, Member, *IEEE*, Jianming Wang, Xiuyan Li, Xiaojie Duan, Ronghua Zhang, Hong Zhang, Yanhe Ma, Huaxiang Wang, *Senior Member, IEEE*, Jiabin Jia, *Senior Member, IEEE*

***Abstract*—Motion tracking is an effective approach for the management of respiratory motion during the medical imaging process, which has always been a major concern in diagnostic imaging, interventional, and non-invasive therapy. However, the low imaging speed of traditional medical imaging techniques limits the practical application of real-time motion tracking. Electrical impedance tomography (EIT) is proved to be an effective tool for continuous monitoring of lung activity/status. However, the respiratory motion has never been studied in the medical EIT field before. In this paper, preliminary research of lung movement during the respiratory process is first studied based on EIT. Multi-ring electrode thorax models under different respiratory statuses were constructed to obtain simulation data of EIT. A modified TV algorithm is used for the estimation of lung volume and movement based on 3D EIT images, which improve the quality of reconstruction by approximately 30% and 20% compared with the traditional Tikhonov method and the total variation (TV) method, respectively. Both simulations and experiments were conducted to show the potential of respiratory motion tracking through 3D EIT reconstruction.**

***Index Terms*—Electrical impedance tomography, Respiratory motion, Total variation, Image reconstruction.**

I. Introduction

DEVELOPMENTS in imaging technology have opened up an increasingly wide range of potential applications for medical images, such as diagnosis, treatment planning, and image-guided interventions[1]-[3]. According to the dynamic characteristics of the human body, organ motion has to be considered during the imaging process. The lung respiration motion has been studied to estimate focus movement for accurate diagnosis and interventional/non-invasive therapy[4], [5]. Over the past few years, there has been significant interest in respiratory motion tracking management using medical imaging devices such as ultrasound tomography (UT), positron emission tomography (PET), computed tomography (CT) and magnetic resonance imaging(MRI) [6]-[10]. Due to the low imaging speed or radiological hazard of traditional imaging techniques, the common method is to evaluate the motion based on several specific statuses during the breathing cycle, e.g. the end-inspiration and end-expiration (peak-to-peak) statuses[11], [12]. However, the temporal resolution of the image is low due to a lack of accurate dynamic information. 4D medical imaging technology provides the availability of dynamic tracking for respiratory motion [13];nevertheless, it can be difficult to image the motion of interest directly during the imaging procedure. Surrogate or marker is always used and the regular variation of breathing pattern has to be assumed to simplify the imaging process [14].

Electrical impedance tomography (EIT) is a relatively new technique intended for imaging the electrical conductivity distribution within a human body [15-18]. EIT could provide variation of conductivity distribution for lung during the breathing process [19], [20]. Compared with traditional medical imaging techniques, EIT is a non-invasive, bedside radiation-free imaging modality and could continuously monitor lung function [21]-[26]. As a dynamic medical imaging technique, it is an ideal and promising method to monitor lung movements. However, most of the applications and researches for lung EIT only focus on the estimation of the lung volume, i.e. ventilation and perfusion based on reconstructed images [27]-[30]. The intrathoracic organ motion, which is an essential parameter based on dynamic EIT reconstruction hasn't been considered before.

In this paper, the respiratory motion of lung is first monitored based on EIT reconstructions. The real 3D thorax models for specific statuses, i.e. end-expiration and end-inspiration, are built based on CT slices for the simulation study. Inspired by edge-preserving and scale-dependent properties of total variation (TV)regularization, a modified split-Bregman total variation(MTV) algorithm is proposed for 3D reconstruction to improve the estimation accuracy of lung movement. Lung characteristics and respiratory motion are studied based on 3D lung EIT images of different respiratory statuses.

This work was supported in part by the National Natural Science Foundation of China (Grants No. 62072335, No. 62071328, No. 61903273, and No. 61872269), in part by the Natural Science Foundation of Tianjin City (Grant No. 18JCYBJC85300) and in part by Tianjin Science and Technology Plan Project (19PTZWHZ00020) (Corresponding author: Jianming Wang)

Q. Wang are with the School of Life Science, Tianjin Polytechnic University, Tianjin 300387, China (e-mail: wangqitju@163.com)

J. Wang is with the School of Computer Science and Technology, Tianjin Polytechnic University, Tianjin 300387, China (e-mail: wjm_tjpu@163.com)

X. Li and X. Duan are with the School of Electronics and Information Engineering, Tianjin Polytechnic University, Tianjin 300387, China (e-mail: lixiuyan@tjpu.edu.cn)

R. Zhang is with the School of Artificial Intelligence, Tianjin Polytechnic University, Tianjin 300387, China (e-mail: rh_zhang_2005@163.com)

H. Zhang and Y. Ma is with the Medical Imaging Department, Tianjin Chest Hospital, Tianjin 300222, China (e-mail:yuxinli72@163.com)

H. Wang is with the School of Electrical Engineering and Automation, Tianjin University, Tianjin 300072, China (e-mail: hxwang@tju.edu.cn).

J. Jia is with the Agile Tomography Group, School of Engineering, Institute for Digital Communications, The University of Edinburgh, Edinburgh EH9 3JL, U.K. (e-mail: jiabin.jia@ed.ac.uk)

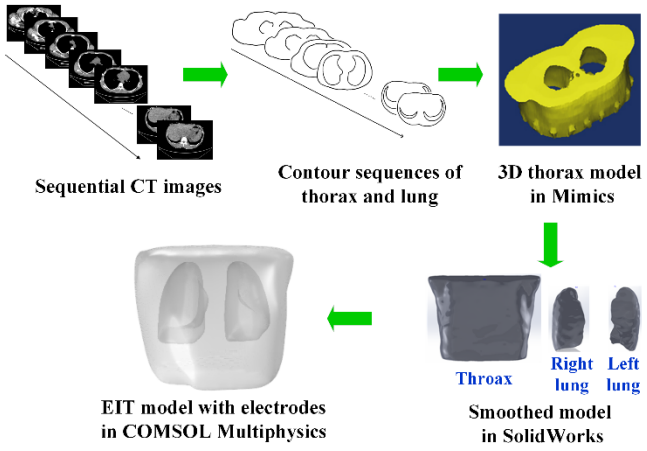

Fig. 1.Procedure of constructing the 3D thorax model.

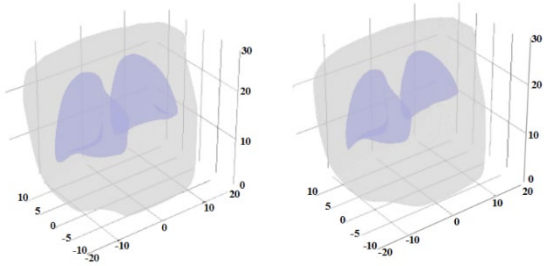

Fig. 2. 3D thorax model under two respiratory statuses (unit: cm).(a)end-inspiration status; (b) end-expiration status.

The experiments are also conducted to verify the effectiveness of the new method. Both simulation and experimental results show that EIT reconstruction of lung is capable for evaluation of respiratory motion.

The paper is organized as follows. In Section Ⅱ, the basic mathematical model based on TV regularization for EIT is briefly described. Realistic 3D thorax models under different respiratory statuses are built and EIT forward problems are solved in Section Ⅲ. Section Ⅳ introduces the modified TV regularization method and its solution based on the split-Bregman iteration method. In Section Ⅴ, numerical experiments are designed for 2D and 3D EIT lung imaging based on the MTV method with selected parameters. The respiratory motions between end-expiration and end-inspiration statuses are discussed. 3D lung image reconstruction and evaluation of respiratory motion through real data are conducted in Section Ⅵ. Finally, the conclusions are drawn in Section Ⅶ.

II. Basic of EIT Reconstruction

The difference imaging method is always used in EIT, which can be expressed as

$$V = F(\sigma) + e \tag{1}$$

where F is the nonlinear forward operator, e is measurement noise, σ is the conductivity differences concerning the reference and V is the measured boundary voltage variations. In practice, equation (1) is linearized as [31]

$$V = J\sigma + e \tag{2}$$

where V is the measured voltage sequence, J is the sensitivity matrix, σ is the conductivity variation vector between the object and reference fields. In this paper, the thorax model with evenly distributed conductivity is used as the reference distribution.

To estimate the conductivity distribution from boundary voltages, the inverse problem needs to be solved. A commonly used method to solve this problem is reformulating it into a Tikhonov regularization problem [32]

$$\arg\min_{\sigma}\{\|J\sigma - V\|_2^2 + \lambda\|\sigma\|_2^2\} \tag{3}$$

whereλ is the regularization parameter. The Tikhonov method is L2 regularization and always prone to get smooth solutionσ. Hence blurred information are introduced into piecewise-constant reconstruction models. To preserve sharp details in reconstruction, TV regularization is incorporated into the EIT model [33], leading to

$$\arg\min_{\sigma}\{\|J\sigma - V\|_2^2 + \lambda\|\sigma\|_{TV}\} \tag{4}$$

where the TV-norm for a 3D model is defined as

$$\|\sigma\|_{TV} = \sum_{i,j,k}\sqrt{\left|(\nabla_x\sigma)_{i,j,k}\right|^2 + \left|(\nabla_y\sigma)_{i,j,k}\right|^2 + \left|(\nabla_z\sigma)_{i,j,k}\right|^2} \tag{5}$$

$$(\nabla_x\sigma)_{i,j,k} = \sigma_{i+1,j,k} - \sigma_{i,j,k}$$
$$(\nabla_y\sigma)_{i,j,k} = \sigma_{i,j+1,k} - \sigma_{i,j,k}$$
$$(\nabla_z\sigma)_{i,j,k} = \sigma_{i,j,k+1} - \sigma_{i,j,k}$$

where $(\nabla_x\sigma)$, $(\nabla_y\sigma)$ and $(\nabla_z\sigma)$ are the first-order local differences in the x, y and z dimension, respectively. The indexes i,j, and k refer to elements in the finite element mesh. In traditional TV solution, a smoothing parameter ε [34] is always introduced to solve the nondifferentiability at the origin:

$$\|\sigma\|_{TV,\varepsilon} = \sum_{i,j,k}\sqrt{\left|(\nabla_x\sigma)_{i,j,k}\right|^2 + \left|(\nabla_y\sigma)_{i,j,k}\right|^2 + \left|(\nabla_z\sigma)_{i,j,k}\right|^2 + \epsilon}. \tag{6}$$

III. 3D Model Construction for EIT Forward Problem

A 3D thoracic model of a woman aged 56, has been developed based on the CT scans. Besides, since the paper focuses on lung movement, the model has been simplified by including only the lungs inside the thorax. The procedure of constructing a realistic 3D thorax model is shown in Fig. 1. The contours of lungs and thorax are extracted based on the maximum inter-class variance algorithm[35] and stacked to obtain the preliminary model of the thorax in Mimics®. In order to obtain a stable solution in the forward problem, SolidWorks® is used to smooth the model. Finally, the lung models are combined with the thorax model in COMSOL Multiphysics® to solve the forward problem.

In order to study the respiratory motion for lung EIT, the 3D thorax model at two specific statuses, namely end-inspiration and end-expiration, are established for the reconstruction of human EIT data in this paper, as shown in Fig. 2. The conductivity of lung tissue at the end-expiration condition and end-inspiration conditions are set to $\sigma_{exp} = 0.12$ S/m and $\sigma_{insp} = 0.06\,S/m$, respectively. The conductivity of other tissues not belonging to the lung is set to $\sigma_{bkg} = 0.48$ S/m [36], [37].

To obtain the 3D reconstruction result, the image could be reconstructed onto multiple voxel layers perpendicular to the z-axis with the measurements from multi-ring electrode planes.

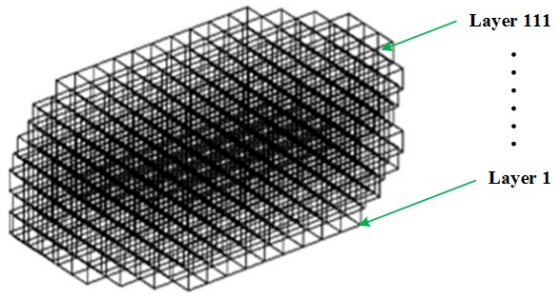

Fig. 3.Voxel mesh for solving inverse problem.

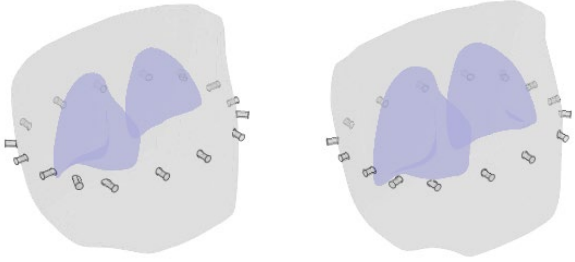

(a) (b)

Fig.4.Thorax model with one EIT electrode ringat layer 56. (a) end-expiration status; (b) end-inspiration status.

Considering the memory limits and speed requirements, there are 111 reconstruction layers for the 3D reconstructed image, i.e. the reconstruction layer separation is 0.25 cm. The 3D mesh for the inverse problem is shown in Fig. 3. The sensing domain is longitudinally divided into 111layers, and each layer has a resolution of 32×32.

According to the 3D effect of the electric field, both on and off plane images could be reconstructed through measured data from one electrode plane. The number of electrode rings is selected heuristically to provide proper coverage of the region of interest. We first test the off-plane influence of reconstructed images with a single electrode ring model which is shown in Fig. 4.The model includes one ring of 16 electrodes. The diameter of each electrode is 1 cm. The adjacent measure pattern with10 mA injected current is used for simulation. 0.1% Gaussian random noise is used to simulate the measurement noise. The reconstructed image on each plane is reconstructed individually based on the Tikhonov method [32].

To evaluate the image quality on each plane, the imaging relative error (*RE*) is adopted:

$$RE_j = \frac{\left\| \sum_{j=1}^{N_j} \sigma_{ij} - \sigma_{ij}^* \right\|_2}{\sum_{i=1}^{N_j} \sigma_{ij}^*}, j = 1,2,3 \cdots M \qquad (7)$$

where σ_{ij} is the reconstructed conductivity of the ith pixel on the jth layer, $\sigma_{ij}^*$is the true one. $N_j$is the number of pixels on the jth layer. M is the number of reconstruction layers.

The relative errors between the reconstructed image and the real conductivity distribution on each layer are calculated and plotted, as shown in Fig. 5. It can be seen that the reconstruction planes far from the electrode plane have higher *RE*s.

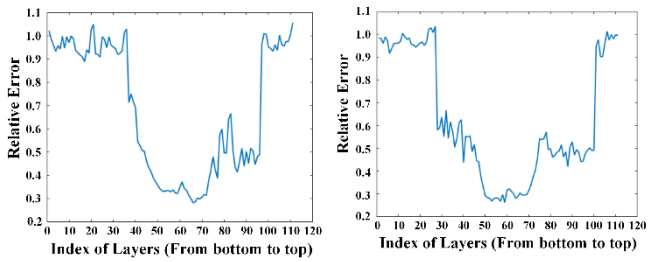

(a) (b)

Fig. 5.Reconstruction *RE*s of each reconstruction layerundertwo respiratory statuses in single electrode ring model.(a) end-inspiration status; (b) end-expiration status.

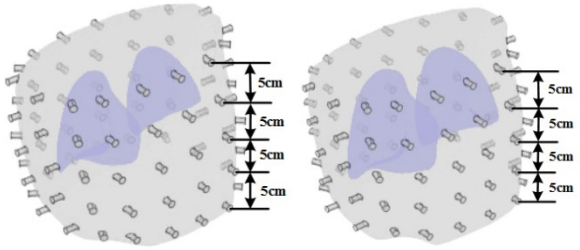

(a) (b)

Fig. 6. 3D thorax models with 5 electrode rings. (a) end-expiration status; (b) end-inspiration status.

To improve spatial resolution on the z-axis and reduce the influence of off-plane objects, we select 20 reconstruction layers 5 cm apart between adjacent rings to cover the whole thorax area. The models with 5 electrode rings are shown in Fig. 6.

IV. The Improved TV Algorithm Based on Split-Bregman Iteration

A. The Mathematical Model of Modified TV Regularization Method

For traditional TV regularization like (6), the behavior of the regularization term is dependent on the parameterϵ. If ϵ is too large, the quadratic smoothing effect will be introduced into TV regularization. Furthermore, the convergence of the inversion is sensitive to the parameterϵ. As a result, the solution of (6) is unstable, and unwanted inversion artifacts are produced. Inspired by the modified total variation (MTV) regularization scheme proposed by Lin and Huang [38] for 2D acoustic and elastic waveform inversion, we apply the MTV regularization scheme to the 3D EIT to preserve sharp boundaries and improve the accuracy of the reconstructed image. The objective function of 3D EIT with the MTV regularization is defined as

$$\arg\min_{\sigma,u}\{\|V - J\sigma\|_2^2 + \lambda_1\|\sigma - u\|_2^2 + \lambda_2\|u\|_{TV}\} \qquad (8)$$

where λ_1 and λ_2 are the regularization parameters, and u is the auxiliary variable.

B. The Solution of the Mathematical Model

The double minimization problem in (8) is solved by the alternating-minimization algorithm. With initial model $u^{(0)} =$

$\sigma^{(0)}$, problem (8) leads to the two minimization sub problems:

$$\sigma^{(k)} = \arg\min_{\sigma}\left\{\|V - J\sigma\|_2^2 + \lambda_1\|\sigma - u^{(k-1)}\|_2^2\right\} \quad (9)$$

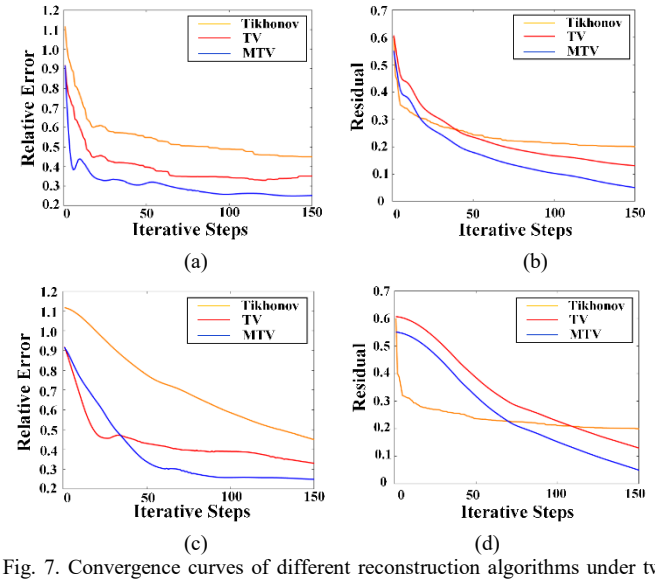

Fig. 7. Convergence curves of different reconstruction algorithms under two respiratory statuses. (a) The relative errors versus iterative steps for three algorithms at end-expiration status; (b) The residuals versus iterative steps for three algorithms at end-expiration status; (c) The relative errors versus iterative steps for three algorithms at end-inspiration status; (d) The residuals versus iterative steps for three algorithms at end-inspiration status.

$$u^{(k)} = \arg\min_{\sigma}\left\{\|\sigma^{(k)} - u\|_2^2 + \lambda_2\|u\|_{TV}\right\} \quad (10)$$

where$k$ is the iteration number. The alternating solution of the two sub problems not only improves the minimization of the residual term, but also enhances the sharpness of reconstruction.

The conjugate gradient method is used to solve the first sub problem iteratively:

$$(J^TJ + \lambda_1 I)\Delta\sigma^{(k)} = J^T(V - J\sigma^{(k)}) - \lambda_1(\sigma^{(k)} - u^{(k-1)}) \quad (11)$$

where $\Delta\sigma^{(k)}$ is the perturbation of the model, and $\sigma^{(k)}$is the conductivity model at the kth iteration.

After calculating the conjugate direction and step length, the model parameters at the current iteration can be updated:

$$\Delta\sigma^{(k+1)} = \sigma^{(k)} + \Delta\sigma^{(k)} \quad (12)$$

The second sub problem is solved using the split-Bregman iterative method, which composes functional splitting and the Bregman distance. In the splitting step, the TV term is decoupled from the residual term. In the Bregman iteration step, the TV term is reformulated with the Bregman distance. The implementation of the split-Bregman iteration is as follows:

A penalty term is added to the functional:

$$\min_{u,w_x,w_y,w_z}\left\{\|\sigma^{(k)} - u\|_2^2 + \lambda_2\|u\|_{TV} + \alpha\|w - \nabla u\|_2^2\right\} \quad (13)$$

where $w \approx \nabla u$. We introduce the Bergman iteration method [39] to solve the unconstrained problem given by

$$\min_{u,w_x,w_y,w_z}\left\{\|\sigma^{(k)} - u\|_2^2 + \lambda_2\|u\|_{\mathrm{TV}} + \alpha\|w - \nabla u - b^k\|_2^2\right\}$$

$$b^{k+1} = b^k + \left(\nabla u^{(k+1)} - w^{(k+1)}\right) \quad (14)$$

where$\|u\|_{\mathrm{TV}}$ is the L_1 term, $\|\sigma^{(k)} - u\|_2^2$ and $\|w - \nabla u - b^k\|_2^2$ are the L2 terms,$b^k$is the auxiliary variables, and $b^0 = 0$.

The L_1 and L_2 components in (14) are split and the problem is optimized to an alternating minimization fashion with the following two sub problems:

$$\min_u\left\{\|u - \sigma^{(k)}\|_2^2 + \alpha\|w^{(k)} - \nabla u - b^k\|_2^2\right\} \quad (15)$$

$$\min_{w_x,w_y,w_z}\{\lambda_2\|u\|_{TV} + \alpha\|w - \nabla u - b^k\|_2^2\}. \quad (16)$$

To minimize (15), the first-order derivative is simply set as zero. The optimal value of u can be obtained by solving the following equation:

$$(I - \alpha\triangle)u^{(k+1)} = \sigma^{(k)} + \alpha\nabla^T(w^{(k)} - b^{(k)}). \quad (17)$$

The generalized shrinkage formula [40] is used to solve the minimization problem in (16):

$$w^{k+1}| = max\left(q^k - \frac{\lambda_2}{2\alpha}, 0\right)\frac{\nabla u^k + b^k}{q^k} \quad (18)$$

where q^k is defined as:

$$q^k = \sqrt{|\nabla_x u^k + b_x^k|^2 + \left|\nabla_y u^k + b_y^k\right|^2 + |\nabla_z u^k + b_z^k|^2}. \quad (19)$$

The procedure of the MTV algorithm for EIT reconstruction is summarized in Algorithm 1.

Algorithm 1 MTV algorithm for EIT reconstruction

Input:$V, J, u^{(0)}$, Tolerance
Output:$\sigma^{(k)}$
1: Initialize $k = 0$;
2: while $\|\sigma - \sigma^{(k)}\|_2^2 > Tolerance$**do**
3: Solve (11) for $\sigma^{(k)}$ according to equation (9)
4: Solve (13) for $u^{(k)}$ according to equation (10)
5: $k \leftarrow k + 1$;
6: **end while**

There is no need for the smoothing parameter ϵ in the MTV regularization scheme. As a result, the robustness of the EIT reconstruction problem is improved.

V. Numerical Results

Numerical simulations are performed based on the true thorax 3D model at end-inspiration and end-expiration statuses with five electrode rings constructed in Fig. 6. The MTV method is evaluated for 2D and 3D reconstruction of lung EIT in this section. Furthermore, respiratory movements are analyzed based on the reconstruction results.

A. Selection of Parameters for the MTV Algorithm

The parameter selection for the MTV algorithm is discussed based on numerical simulation. The single electrode ring model constructed in Fig. 4 is used in this section for discussion of the parameters.

1) Iteration Number

We compare the convergence rates of Tikhonov, TV, and MTV regularization schemes in Fig. 7. Iterative reconstruction for both end-inspiration and end-expiration statuses are discussed. To qualify the accuracy of these results, we calculate the *RE* defined in (7) and residual$\|V - J\sigma\|_2^2$for each iteration.

The relative error and the residual curves are also provided in Fig. 7 to compare the convergence rates of the three methods. The relative error curves in Fig. 7(a) and(c) show that the MTV

converges much faster than the other two methods. On the other hand, the residual curves in Fig. 7(b) and (d) demonstrate that the three methods converge significantly different from one another. Considering both the accuracy and efficiency, we select 50 iteration steps empirically for the MTV method.

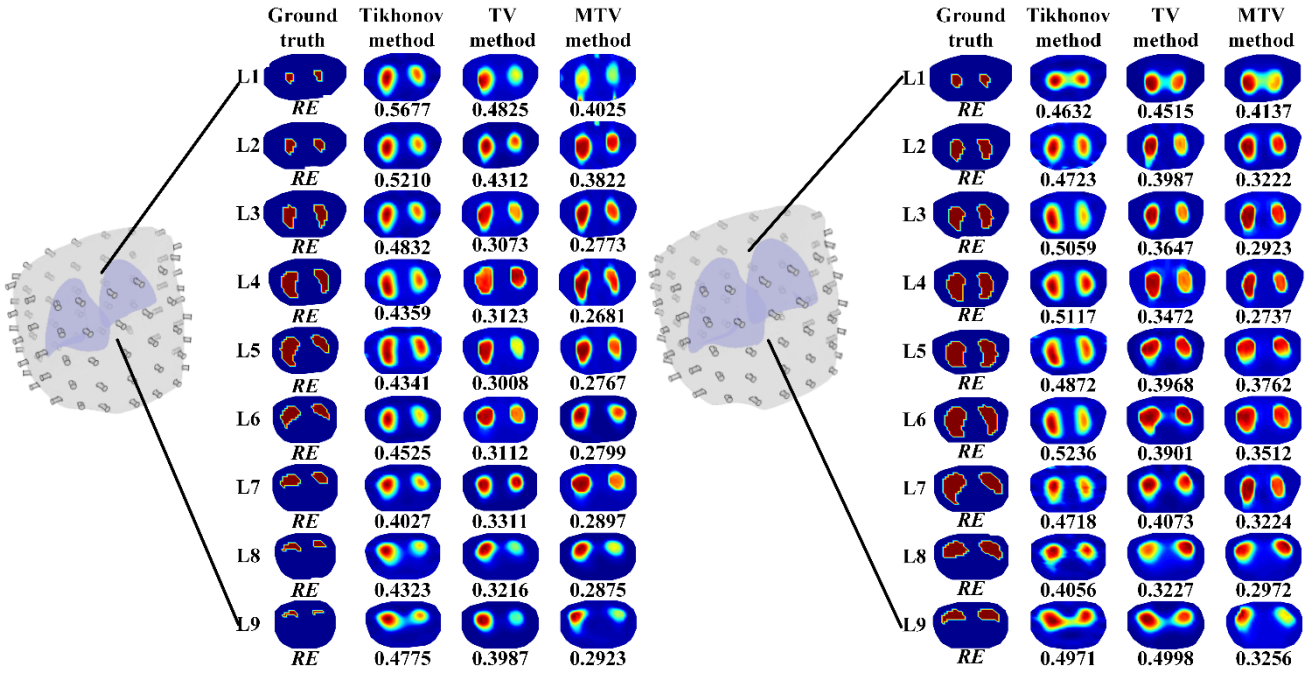

(a) (b)

Fig. 8. 2D lung images reconstructed using three algorithms. The images are given from top to the bottom according to simulation model, which contains lung region. Nine image planes for each respiratory status. (a) Reconstructed images for end-expiration model; (b) Reconstructed images for end-inspiration model.

2) Regularization Parameter

Appropriate regularization parameters are important to obtain accurate inversion results. The regularization parameter λ_1 controls the trade-off between the residual and the Tikhonov regularization terms, the regularization parameter λ_2 balances interface preservation in inversion. In this study, we estimate the regularization parameters λ_1 and λ_2 from several experiments and fix them as $\lambda_1 = \lambda_2 = 0.01$.

As problem (8) is a multiply-constrained regularization problem, we can also adjust λ_1 and λ_2 via L-hypersurface method [41] to produce an acceptable accuracy of reconstruction. Here we propose the L-hypersurface as a multi-dimensional extension of the classical L-curve method. To construct the L-hypersurface, we first introduce the following quantities:

$$z(\lambda_1, \lambda_2) = \|V - J\sigma(\lambda_1, \lambda_2)\|_2^2 \quad (20)$$

$$x_1(\lambda_1, \lambda_2) = \|\sigma(\lambda_1, \lambda_2) - \mu(\lambda_1, \lambda_2)\|_2^2 \quad (21)$$

$$x_2(\lambda_1, \lambda_2) = \|\mu(\lambda_1, \lambda_2)\|_{\mathrm{TV}} \quad (22)$$

where $\sigma(\lambda_1, \lambda_2)$ and $\mu(\lambda_1, \lambda_2)$ are the solutions of problem (8) with any regularization parameters λ_1 and λ_2;

We denote the points where extreme solution norm and extreme residual norm regions start by a and b respectively. The points a and b can be defined as

$$a = \log z(\rho_{min}^2, \rho_{min}^2) \quad (23)$$

$$b_1 = \log x_1(\rho_{max}^2, 0) \quad (24)$$

$$b_2 = \log x_2(0, \rho_{max}^2) \quad (25)$$

where ρ_{min} and ρ_{max} denote the smallest and largest singular values of sensitivity matrix J.

Then we define the distance from the origin $O = (a, b_1, b_2)$ to any point $\beta(\lambda_1, \lambda_2)$ on the L-hypersurface:

$$\beta(\lambda_1, \lambda_2) = ([\log x_1(\lambda_1, \lambda_2)], [\log x_2(\lambda_1, \lambda_2)], [\log z(\lambda_1, \lambda_2)]) \quad (26)$$

$$v(\lambda_1, \lambda_2) = |\log z(\lambda_1, \lambda_2) - a|^2 + |\log x_1(\lambda_1, \lambda_2) - b_1|^2 + |\log x_2(\lambda_1, \lambda_2) - b_2|^2. \quad (27)$$

The optimized parameters could be obtained when $v(\lambda_1, \lambda_2)$ reaches a local minimum, i.e.

$$\lambda_1^*, \lambda_2^* = \arg\min v(\lambda_1, \lambda_2). \quad (28)$$

The solution of equation (28) could be given by iterative algorithm

$$\lambda_1^{(l+1)} = \frac{z(\lambda_1^{(l)}, \lambda_2^{(l)})}{x_1(\lambda_1^{(l)}, \lambda_2^{(l)})} \left(\frac{\log[x_1(\lambda_1^{(l)}, \lambda_2^{(l)})] - b_1}{\log[z(\lambda_1^{(l)}, \lambda_2^{(l)})] - a} \right) \quad (29)$$

$$\lambda_2^{(l+1)} = \frac{z(\lambda_1^{(l)}, \lambda_2^{(l)})}{x_2(\lambda_1^{(l)}, \lambda_2^{(l)})} \left(\frac{\log[x_2(\lambda_1^{(l)}, \lambda_2^{(l)})] - b_2}{\log[z(\lambda_1^{(l)}, \lambda_2^{(l)})] - a} \right) \quad (30)$$

where $\lambda_1^{(l)}$ and $\lambda_2^{(l)}$ are regularization parameters at step l. The algorithms started with appropriate initial regularization parameters $\lambda_1^{(0)}$ and $\lambda_2^{(0)}$ and iterated until the relative change in the iterates is determined to be sufficiently small.

B. 3D Reconstruction Results

EIT images are generated for two respiratory statuses. The lung areas under end-expiration and end-inspiration conditions are divided into 60 and 72 horizontal cut planes respectively. Fig. 8 shows nine specific image levels reconstructed based on different algorithms for each respiratory status. We could see the variations in the 3D patterns show a clear separation of the lung in lower planes and higher planes. On the left, the

simulation models are shown along with the imaging areas, at the right, reconstructed images of nine image planes are given. We could see from Fig. 8 that all of the three algorithms could reflect the variation of the lung region in the 3D dimension. Although the TV and MTV methods have the edge-preserving effect, the MTV method could better distinguish the lung volume between end-expiration and end-inspiration statuses.

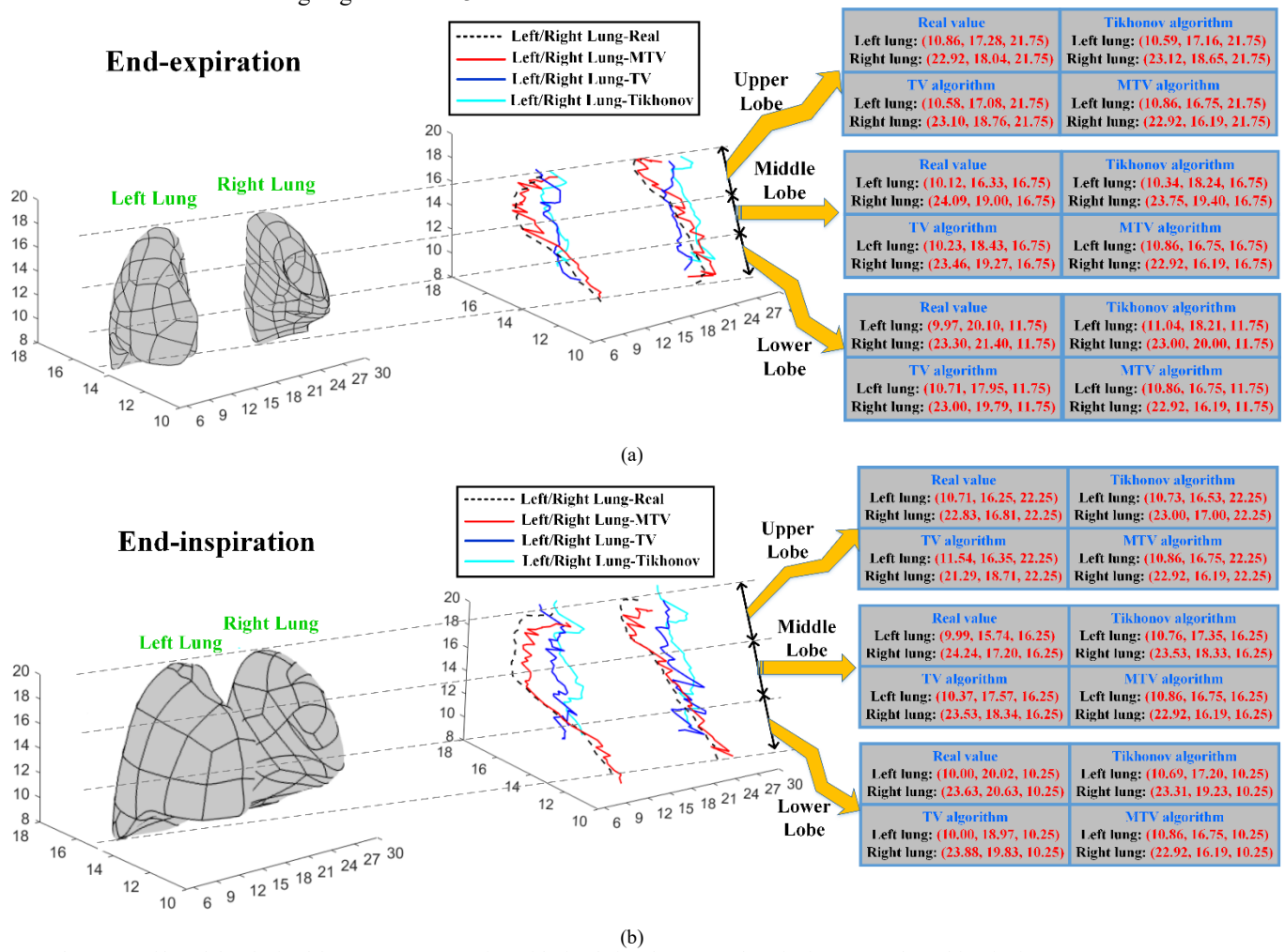

Fig. 10. The center of lung lobe obtained from EIT reconstruction with simulation data. (a) end-expiration status. (b) end-inspiration status.

In Fig. 9, 3D reconstructions of lung images are achieved utilizing the Tikhonov algorithm, TV algorithm, and MTV algorithm, respectively. In order to explore the structure inside the thorax, we display the coronal and sagittal cut planes of the 3D reconstructed images. According to the results shown in Fig. 9, the 3D reconstructed images can suggest the variation of lung volumes under different respiratory statuses. The reconstruction results of Tikhonov regularization algorithm produce smooth solutions, while the reconstruction results of the MTV regularization improve the edge-preserving performance in the inversion result compared with the Tikhonov and traditional TV methods. Equation (7) is modified to evaluate the quality of 3D reconstructed images:

$$RE = \frac{\left\| \sum_{j=1}^{M} \sum_{i=1}^{N_j} (\sigma_{ij} - \sigma_{ij}^*) \right\|_2}{\sum_{j=1}^{M} \sum_{i=1}^{N_j} \sigma_{ij}^*}. \quad (31)$$

The computational time for different methods is shown in Table Ⅰ. The reconstruction is performed on a PC configured for 2.7GHz GPU, 8GB of memory. The reconstruction time of the MTV method is longer than that of the Tikhonov method.

TABLEI
COMPARISON OF THREE METHODS IN TERMS OF COMPUTATIONAL TIME

Respiratory status	Computational time (ms)		
	Tikhonov method	TV method	MTV method
End-expiration	323	700	574
End-inspiration	354	723	586

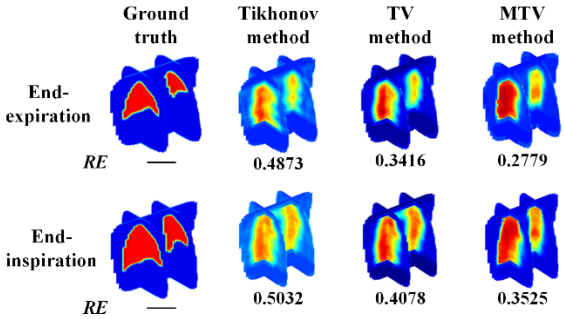

Fig. 9. 3D lung reconstruction results based on simulation data.

TABLE Ⅱ
COMPARISON OF *LRRs* BASED ON SIMULATION DATA

	Real	Tikhonov ($error_{LRR}$)	TV($error_{LRR}$)	MTV($error_{LRR}$)
End-expiration	0.0753	0.0962**(0.0209)**	0.0838 **(0.0085)**	0.0740**(-0.0013)**
End-inspiration	0.1294	0.1763**(0.0469)**	0.1487 **(0.0193)**	0.1273 **(-0.0021)**

TABLE Ⅲ
VARIABILITY OF RESPIRATORY MOTION FROM END-EXPIRATION TO END-INSPIRATIONSTATUSES

Localization	Algorithm	Lobe/ Side	Respiratory motion (cm) X (Lateral)	Y (Anteroposterior)	Z (Craniocaudal)	3D
Upper lobe	Real value	L	-0.15	-1.03	0.5	1.15
		R	-0.09	-1.23	0.5	1.33
	Tikhonov **(Error)**	L	0.14 **(0.29)**	-0.73 **(0.60)**	0.5	0.90 **(-0.25)**
		R	-0.81 **(-0.72)**	-0.05 **(1.18)**	0.5	0.95 **(-0.38)**
	TV **(Error)**	L	0.11 **(0.26)**	-0.63 **(0.50)**	0.5	0.81 **(-0.34)**
		R	-0.24 **(-0.15)**	-1.65 **(-0.42)**	0.5	1.74 **(0.41)**
	MTV **(Error)**	L	0.04 **(0.11)**	-0.88 **(0.15)**	0.5	1.01 **(-0.14)**
		R	-0.22 **(-0.13)**	-1.35 **(-0.12)**	0.5	1.46 **(0.13)**
Middle lobe	Real value	L	-0.13	-0.59	-0.5	0.78
		R	0.15	-1.8	-0.5	1.87
	Tikhonov **(Error)**	L	0.12 **(0.25)**	-0.89 **(-0.30)**	-0.5	1.03 **(0.25)**
		R	-0.22 **(-0.37)**	-1.07 **(0.73)**	-0.5	1.20 **(-0.67)**
	TV **(Error)**	L	0.08 **(0.21)**	-0.86 **(-0.27)**	-0.5	1.00 **(0.22)**
		R	0.07 **(-0.08)**	-0.93 **(0.87)**	-0.5	1.06 **(-0.81)**
	MTV **(Error)**	L	-0.07 **(0.06)**	-0.72 **(-0.13)**	-0.5	0.88 **(0.10)**
		R	0.11 **(-0.04)**	-1.51 **(0.29)**	-0.5	1.59 **(-0.28)**
Lower lobe	Real value	L	0.03	-0.09	-1.5	1.50
		R	0.33	-0.77	-1.5	1.72
	Tikhonov **(Error)**	L	-0.71 **(-0.74)**	1.02 **(1.11)**	-1.5	1.95 **(0.45)**
		R	0.81 **(0.48)**	0.04 **(0.81)**	-1.5	1.71 **(-0.01)**
	TV **(Error)**	L	-0.35 **(-0.38)**	-1.01 **(-0.92)**	-1.5	1.84 **(0.34)**
		R	0.63 **(0.3)**	-0.28 **(0.51)**	-1.5	1.65 **(-0.07)**
	MTV **(Error)**	L	0.12 **(0.09)**	1.21 **(0.19)**	-1.5	1.93 **(0.43)**
		R	0.31 **(-0.02)**	0.12 **(0.08)**	-1.5	1.54 **(-0.18)**

C. Analysis of 3D EIT Reconstruction Results

1) Lung Volumes

One of the main advantages of 3D EIT is that it has the potential to capture regional lung activity inhomogeneities in a volume. In order to analyze lung volume based on 3D EIT data, the lung volumes during end-inspiration and end-expiration statuses are studied based on lung regional ratio (*LRR*). The *LRR* values based on 3D reconstructed images for two respiratory conditions are calculated according to (32) and shown in Table Ⅱ.

$$LRR = \frac{VA}{TA+VA} \quad (32)$$

where *VA* is the ventilation area and *TA* is the thorax area apart from the lungs. The *LRR*s based on reconstructed images are compared to the *LRR*s based on real images by calculating the errors.

$$error_{IRR} = LRR_{recons} - LRR_{real} \quad (33)$$

where LRR_{recons} is *LRR* based on the reconstruction results, and LRR_{real} is the real *LRR* which is obtained through the simulation model built by CT scan in Section Ⅲ.

From Table Ⅱ, we can see that lung volume increases as the end-expiration to end-inspiration amplitude of conductivity distribution changes. Furthermore, the *LRR* parameters estimated based on the reconstruction results also demonstrate that the MTV method is most suitable for lung ventilated volume calculation.

2) Respiratory Movement

Theoretically, reconstructed images can suggest the variation of respiratory movement between end-inspiration and end-expiration statuses. Numerical calculations of lung positions detected by 3D lung EIT images based on simulation data are presented. We evaluate the position of the lung with the aid of the central position of the lung area in each slice. In order to obtain the central position of the lung, the center of each lung lobe in the 2D slice is calculated based on image processing: Firstly, the lung area of each slice is extracted. The lung region is extracted from the whole thorax region through the maximum inter-class variance algorithm [42]. Then the geometric centers of the two lung lobes are found [43]. Both the lung EIT images of end-inspiration and end-expiration are processed, so that the position of the lung in each slice under two respiratory conditions could be obtained. Fig.10 brings lung positions from image slices together as curve graphs to make a comparison. The black dotted line indicates the true positions of the 3D lung image, and others are given by the quantitative results from reconstructed images with different algorithms. Comparing the lung positions obtained from different reconstruction algorithms, the ones calculated based on the MTV image is closer to the true position, with others showing a little further deviation. The results suggest that the MTV method would be feasible to explore the information about 3D lung EIT.

According to the related studies based on CT images, the lung area is separated into 3 parts, namely the upper lobe, middle lobe, and lower lobe. The lung positions are then averaged over all slices for each lobe.

The positions of different lobe under two respiratory conditions are shown in Fig. 10.

The respiratory movement between end-inspiration status and end-expiration status are calculated in three perspectives,

$$MOV_i = PIN_{vi} - PEX_{vi} \quad (34)$$

where *i*=1,2,3 is the index of a lung lobe, *v* =1,2,3 is the index of perspective, *MOV* is respiratory movement, *PIN* and *PEX* are lung positions under end-inspiration and end-expiration statuses, respectively.

According to the respiratory movement on three perspectives, the 3D movement is calculated,

$$MOV_{3D_i} = \sqrt{\sum_{v=1}^{3} MOV_{vi}^2}. \quad (35)$$

The respiratory motion parameters calculated from the reconstructed images with different algorithms are shown in Table III. The error between the reconstruction and real value is calculated,

$$error_{MOV} = MOV_{recons} - MOV_{real} \quad (36)$$

where MOV_{recons} is *MOV* based on the reconstruction results, and MOV_{real} is real *MOV* obtained from simulation model.

From Table Ⅲ, we could see that the positions of pulmonary structures vary during respiratory process according to conductivity distribution. For 3D results, the middle lobe and lower lobe have larger movement than the upper lobe. Furthermore, there are differences between inspiration and expiration in three axial directions. Lung motion was observed in anteroposterior and craniocaudal directions, with only very limited lateral movements. The trend of the lung motion variation based on reconstruction results is consistent with the real ones. The MTV algorithm could give the most accurate respiratory motion results because of the best image quality.

VI. Experimental Results

Experiments were conducted with thorax shape models using the TJPU-EIT system (see Fig. 11). We 3D printed two sets of models for two respiratory conditions, as shown in Fig. 12. Each model contains a clear thorax phantom and two white lung phantoms according to the geometric dimension of the simulation model discussed in Section Ⅲ. As a result, the capacity of the system is about 23 liters according to the volume of the thorax. 5 electrode rings similar to the simulation study were distributed on the inner surface of the thorax phantom. There are 16 round electrodes made of titanium alloy in each electrode ring. The thorax phantom was filled with a saline solution of conductivity0.32 S/m.

The lung phantoms are hung in the saline water according to the positions in simulation models. Refer to the developed EIT systems applied for pulmonary ventilation and perfusion, 5 mA current was injected adjacently at frequency 50kHz[44]-[46] and the adjacent voltage data was measured. For each pulmonary model, both the reference field (only thorax phantom filled with saline water) and the object field (the lung phantoms immersed in saline water) are tested for difference imaging.

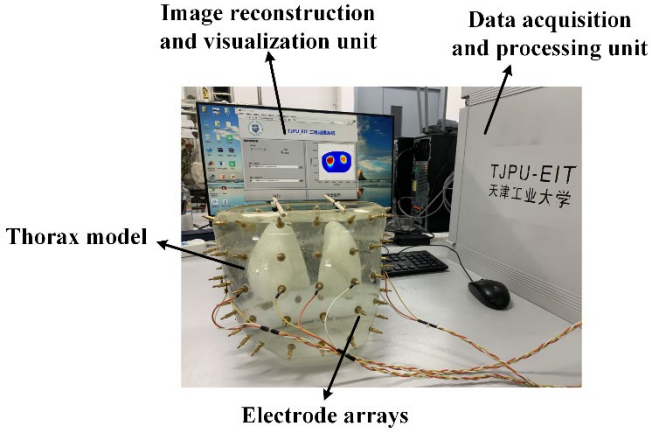

Fig. 11 TJPU-EIT system for experiment

TABLE Ⅴ
COMPARISON OF *LRRs* BASED ON EXPERIMENTAL DATA

	Real	Tikhonov($error_{LRR}$)	TV($error_{LRR}$)	MTV($error_{LRR}$)
End-expiration	0.0753	0.1076(0.0323)	0.0907(0.0154)	0.0671(-0.0082)
End-inspiration	0.1294	0.1863(0.0569)	0.1552(0.0258)	0.1173(-0.0121)

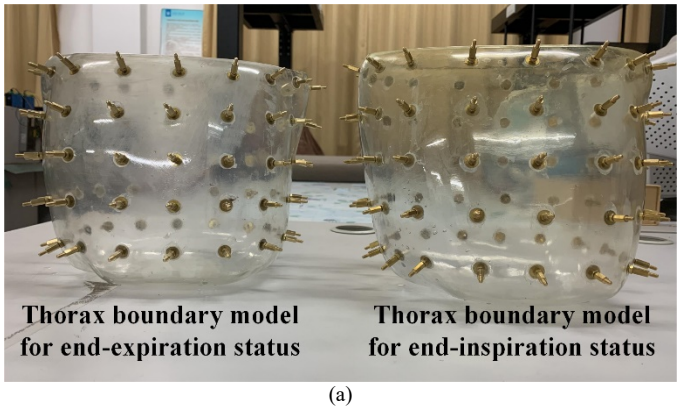

(a)

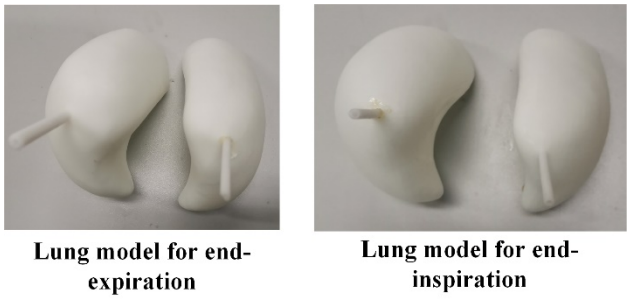

(b)

Fig.12. 3D printed phantom of the thorax. (a) Thorax cavity. (b) Lungs.

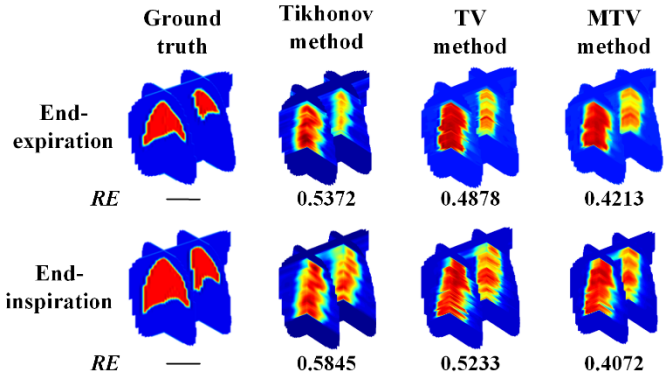

Fig.13.3D lung reconstruction results based on experimental data.

TABLE Ⅳ
COMPARISON OF EXPERIMENTAL RECONSTRUCTION RESULTS IN TERMS OF SYSTEM RESPONSE TIME

Respiratory status	Computational time (ms)	
	TV method	MTV method
End-expiration	723	573
End-inspiration	755	598

A full set of measurements $V^{j,k}$, j, k = 1,…,16 for each electrode ring is provided by the TJPU-EIT system. However, only 16×13 measurements ($V^{j,k}$ with $|j-k|>1$) are used for reconstruction, in order to avoid the errors and unknown contact impedance produced by current-driven electrodes.

Similar to simulation, the measurements from the five rings cover the reconstruction of 111 slices for the whole thorax. The reconstruction results of TV and MTV methods are compared in Fig. 13. We could distinguish between inspiration and expiration through images reconstructed based on all of the three methods. However, compared with the results obtained by the MTV method, more artifacts and discontinuities can be observed in the recovered lung region by the other two methods.

The response time of the practical EIT system includes data acquisition time and image reconstruction time. The response time for experimental reconstruction is shown in TableⅣ. The MTV method has better real-time performance than the TV method. The data acquisition and transmission time, i.e. the time to measure and communicate one tomography measurement frame through to the reconstruction unit is about 2.5 ms, which is only a small fraction of system response time. That means the response time of the system has the potential to be improved with high-performance reconstruction algorithm and computing equipment.

The *LRR* and respiratory movement are also calculated according to the experimental 3D reconstruction results, as shown in Table Ⅴ and Table Ⅵ respectively.

As expected, the estimated respiratory parameters with the MTV reconstruction results have the lowest errors. It demonstrates that 3D EIT not only give images and ventilation area of lungs, but also could provide respiratory motion information.

TABLE VI
VARIABILITY OF RESPIRATORY MOTION FROM END-EXPIRATION TO END-INSPIRATION STATUSES BASED ON EXPERIMENTAL DATA

Localization	Algorithm	Lobe/ Side	Respiratory motion (cm)			
			X (Lateral)	Y (Anteroposterior)	Z (Craniocaudal)	3D
Upper lobe	Real value	L	-0.15	-1.03	0.5	1.15
		R	-0.09	-1.23	0.5	1.33
	TV (Error)	L	0.23 (0.38)	-0.87 (0.16)	0.5	1.03 (-0.12)
		R	-0.37 (-0.28)	-1.79 (-0.56)	0.5	1.89 (0.56)
	MTV (Error)	L	-0.02 (0.13)	-0.97 (0.06)	0.5	1.09 (-0.06)
		R	-0.28 (-0.19)	-1.15 (-0.08)	0.5	1.28 (-0.05)
Middle lobe	Real value	L	-0.13	-0.59	-0.5	0.78
		R	0.15	-1.8	-0.5	1.87
	TV (Error)	L	0.11 (0.24)	-0.79 (-0.2)	-0.5	0.94 (0.16)
		R	0.03 (-0.12)	-0.92 (-0.33)	-0.5	1.05 (-0.82)
	MTV (Error)	L	-0.11 (0.02)	-0.87 (-0.28)	-0.5	1.01 (0.23)
		R	0.23 (0.08)	-1.41 (0.39)	-0.5	1.51 (-0.36)
Lower lobe	Real value	L	0.03	-0.09	-1.5	1.50
		R	0.33	-0.77	-1.5	1.72
	TV (Error)	L	-0.35 (-0.38)	-0.62 (-0.89)	-1.5	1.83 (0.33)
		R	0.74 (0.41)	-0.16 (0.61)	-1.5	1.68 (-0.04)
	MTV (Error)	L	0.15 (0.12)	-0.31 (-0.22)	-1.5	1.52 (0.02)
		R	0.38 (0.05)	-0.53 (-0.24)	-1.5	1.64 (-0.08)

VII. CONCLUSION AND FUTURE WORK

In this paper, 3D lung EIT is used for investigating respiratory motion. The 3D thorax models of end-inspiration and end-expiration statuses were constructed. The design of electrodes was discussed according to the offline effect based on reconstructed images. The MTV algorithm was proposed for the 3D reconstruction of EIT. The lung volume and movement between end-inspiration and end-expiration were evaluated based on reconstructed images. Both simulation and experiments show that 3D EIT has the potential for respiratory motion tracking; the MTV algorithm could effectively improve the 3D image quality, and hence improve the accuracy of respiratory motion parameters. It demonstrates the potential for further development of EIT in precision medicine measurement.

When detecting the respiratory motion of real human lungs with EIT, there are many issues to be considered according to the specificity of human bodies and limitation of the system. Other tissues and organs next to the lungs could potentially affect the measurements of the proposed EIT system. The EIT reconstructions are also sensitive to the contact impedance between the electrode and skin. As a result, the conductivity properties of related organs should be properly studied for improving the accuracy of measurement. Furthermore, the thorax deformation during breathing should be considered to modify the reconstruction method.

It is still challenge to improve the resolution in time but maintaining the high resolution in space together with not much cost for 3D reconstruction.In future work, accelerated

algorithms, e.g. parallel computation, will be involved in the 3D EIT reconstruction process, in order to meet the requirement respiratory movement estimation under free-breathing status based on dynamic 3D EIT lung images.

REFERENCES

[1] J. Xin, Q. Jiang, X. Chu, L. Xun, S. Yao, K. Li and W. Zhou "Brain medical image fusion using L2-norm-based features and fuzzy-weighted measurements in 2-D Littlewood-Paley EWT domain," *IEEE Trans. Instrum. Meas.*, vol. 69, no. 8, 5900-5913, 2020.

[2] P. M. Shakeel, M. A. Burhanuddin and M. I. Desa, "Lung cancer detection from CT image using improved profuse clustering and deep learning instantaneously trained neural networks," *Measurement*, vol. 145, pp. 702-712, 2019.

[3] B. Sahiner, A. Pezeshk, L. M. Hadjiiski, X. S. Wang, K. Drukker, K. H. Cha, R. M. Summersm and M.L. Giger, "Deep learning in medical imaging and radiation therapy," *Med. Phys.*, vol.46,no.1,pp.e1-e36, 2019.

[4] T. Pengpan, N. D. Smith, W. Qiu, A. Yao, C. N. Mitchell and M. Soleimani, "A motion-compensated cone-beam CT using electrical impedance tomography imaging," *Physiol. Meas.*, vol. 32, no. 1, pp. 19-34, 2011.

[5] F. Preiswerk, V. De Luca, P. Arnold, Z. Celicanin, L. Petrusca, C. Tanner, O. Bieri, R. Salomir and P. C. Cattin, "Model-guided respiratory organ motion prediction of the liver from 2D ultrasound," *Med. Image Anal.*, vol. 18, no. 5, pp. 740-751, 2014.

[6] D. Ottacher, A. Chan, E. Parent and E. Lou, "Positional and Orientational Accuracy of 3-D Ultrasound Navigation System on Vertebral Phantom Study," *IEEE Trans. Instrum. Meas.*, vol. 69, no. 9, pp. 6412-6419, 2020.

[7] C. Chan, J. Onofrey, Y. Jian, M. Germino, X. Papademetris, R. E. Carson and C. Liu, "Non-rigid event-by-event continuous respiratory motion compensated list-mode reconstruction for PET,"*IEEE Trans. Med. Imaging*, vol. 37, no. 2, pp. 504-515, 2018.

[8] N. Alsbou, M. Afify, K. Thapa and I. Ali, "3D smart mobile platform design for modeling motion artifacts in CT imaging of cancer patients,"*I2MTC-IEEE Int. Instrum. Meas. Technol. Conf.*, Houston, TX, 2018

[9] S. Park, R. Farah, S. M. Shea, E. Tryggestad, R. Hales, and J. Lee, "Simultaneous tumor and surrogate motion tracking with dynamic MRI for radiation therapy planning," *Phys. Med. Biol.*, vol. 63, no. 2, 2018.

[10] N. Abramov, M. Fradkin, L. Rouet and H. A. Wischmann, "Configurable real-time motion estimation for medical imaging: application to X-ray and ultrasound," *J. Real-Time Image Pr.*, vol. 13, no. 1, pp. 147-160, 2017.

[11] H. Dai, L. Dong, B. Lv, Y. Chen, S. Song and S. Su, "Feasibility Study of Permanent Magnet-Based Tumor Tracking Technique for Precise Lung Cancer Radiotherapy," *IEEE Trans. Instrum. Meas.*, vol. 70, 4002010, 2021

[12] C.Hui, Z. Wen, B. Stemkens, R. H. N. Tijssen, C. A. T. Van Den Berg, K. P. Hwang, and S. Beddar, "4D MR imaging using robust internal respiratory signal," *Phys. Med. Biol.*, vol. 61, no. 9, pp. 3472-3487, 2016.

[13] L. Mancini, G. Kourousias, F. Bille, F. De Carlo and A. Fidler, "About a method for compressing x-ray computed microtomography data," *Meas. Sci. Technol.*, vol. 29, no. 4, 044002, 2018.

[14] C. Cavedon, "Real-time control of respiratory motion: Beyond radiation therapy," *Phys. Med.*, vol. 66, pp. 104-112, 2019.

[15] S. Liu, R. Cao, Y. Huang, T. Ouypornkochagorn and J. Jia, "Time Sequence Learning for Electrical Impedance Tomography Using Bayesian Spatiotemporal Priors," *IEEE Trans. Instrum. Meas.*, vol. 69, no. 9, pp. 6045-6057, 2020

[16] S. Hannan, K. Aristovich, M. Faulkner, J. Avery, M. C. Walker, and D. S. Holder, "Imaging slow brain activity during neocortical and hippocampal epileptiform events with electrical impedance tomography," *Physiol. Meas.*, vol. 42, no. 1, 014001, 2021.

[17] E. K. Murphy, A. Mahara, X. T. Wu and R. J. Halter, "Phantom experiments using soft-prior regularization EIT for breast cancer imaging," *Physiol. Meas.*, vol.38,no.6,pp. 1262-1277, 2017.

[18] Z. Chen, Y. Yang and P. O. Bagnaninchi, "Hybrid Learning-Based Cell Aggregate Imaging With Miniature Electrical Impedance Tomography," *IEEE Trans. Instrum. Meas*., vol. 70, 4001810, 2021.

[19] D. Liu, D. Smyl and J. Du, "Nonstationary Shape Estimation in Electrical Impedance Tomography Using a Parametric Level Set-Based Extended Kalman Filter Approach," *IEEE Trans. Instrum. Meas.*, vol. 69, no. 5, pp. 1894-1907,2020.

[20] M. C. Bachmann, C. Morais, G. Bugedo, A. Bruhn, A. Morales, J. B. Borges, E. Costa and J. Retamal, "Electrical impedance tomography in acute respiratory distress syndrome," *Crit. Care*, vol.22,no.1,pp. 263,2018.

[21] Y. Fu, C. Morais, R. Zou, S. Wang, J. Wen, L. Rong, M. Tang, B. Yu, F. Cen, Z. Zhao, I. Frerichs, A. Adler, Y. Liu and L. Liu, "Monitoring bronchoalveolar lavage with electrical impedance tomography: first experience in a patient with COVID-19,"*Physiol. Meas.*, vol.41,no.8, 085008,2020.

[22] S. Ren, K. Sun, C. Tan and F. Dong, "A two-stage deep learning method for robust shape reconstruction with electrical impedance tomography,"*IEEE Trans. Instrum. Meas*., vol. 69, no. 3, 8989855,2020.

[23] Z.Zhao, R. Fischer, I. Frerichs, U. Mueller-Lisse and K. Moller, "Regional ventilation in cystic fibrosis measured by electrical impedance tomography," *J. Cyst. Fibrosis*,vol.11,no.5,pp.412-418,2012.

[24] G. Hahn, J. Niewenhuys, A. Just, T. Tonetti, T. Behnemann, F. Rapetti, F. Collino, F. Vasques, G. Maiolo, F. Romitti, L. Gattinoni, M. Quintel and O. Moerer, "Monitoring lung impedance changes during long-term ventilator-induced lung injury ventilation using electrical impedance tomography," *Physiol. Meas.*, vol. 41, no. 9, 095011, 2020.

[25] M. M. Mellenthin, J. L. Mueller, E. D. L. B. de Camargo, F. S. de Moura, T. B. R. Santos, R. G. Lima, S. J. Hamilton, P. A. Muller and M. Alsaker, "The ACE1 Electrical Impedance Tomography System for Thoracic Imaging," *IEEE Trans. Instrum. Meas*, vol. 68, no. 9, pp. 3137-3150, 2019.

[26] B. K. Walsh and C. D. Smallwood, "Electrical impedance tomography during mechanical ventilation", *Resp. Care*, vol.61, no.10, pp.1417-1424, 2016.

[27] X. Li, X. Chen, Q. Wang, J. Wang, X. Duan, Y. Sun and H. Wang, "Electrical-impedance-tomography imaging based on a new three-dimensional thorax model for assessing the extent of lung injury," AIP Adv., vol. 9, no. 12, 125310, 2019.

[28] J. Wagenaar and A. Adler, "Electrical impedance tomography in 3D using two electrode planes: characterization and evaluation," *Physiol. Meas.*, vol. 37, no. 6, pp. 922-937, 2016.

[29] M. Kircher, G. Elke, B. Stender, M. Hernandez Mesa, F. Schuderer, O. Dollel, M. K. Fuld, A. F. Halaweish, E. A. Hoffman, N. Weiler and I. Frerichs, "Regional lung perfusion analysis in experimental ARDS by electrical impedance and computed tomography," *IEEE Trans. Med. Imaging*, vol. 40, no. 1, pp. 251-261, 2021.

[30] W. Li,J. Xia, G. Zhang, H. Ma, B. Liu, L. Yang, Y. Zhou, X. Dong, F. Fu and X. Shi, “Fast high-precision electrical impedance tomography system for real-time perfusion imaging,” *IEEE Access*, vol.7, no. 2019, pp.61570-61580,2019.

[31] Q. Wang, Z. Lian, Q. Chen, Y. Sun, X. Li, X. Duan, Z. Cui and H. Wang, "Accelerated reconstruction of electrical impedance tomography images via patch based sparse representation," *Rev. Sci. Instrum.*, vol. 87, no. 11, 114707, 2016.

[32] Z. Wang, S. Yue, H. Wang and Y. Wang, "Data preprocessing methods for electrical impedance tomography: a review," *Physiol. Meas.*, vol. 41, no. 9, 095011, 2020.

[33] A. Borsic, B. M. Graham, A. Adler and W. R. B. Lionheart, “In vivo impedance imaging with total variation regularization,” *IEEE Trans. Med. Imaging*,vol.29,no.1,pp.44-54,2010.

[34] G. Gonzalez, J. M. J. Huttunen, V. Kolehmainen, A. Seppanen and M. Vauhkonen, “Experimental evaluation of 3D electrical impedance tomography with total variation prior,” Inverse Probl. Sci. Eng., vol.24, no.8, pp.1411-1431, 2016.

[35] Y. Yang, H. C. Wu and J.Jia, “Image reconstruction for electrical impedance tomography using enhanced adaptive group sparsity with total variation,” *IEEE Sensors J.*,vol.17,no.17,pp.5589-5598,2017.

[36] B. Schullcke, S. Krueger-Ziolek, B. Gong, R. A. Jorres, U. Mueller-Lisse and K. Moeller, “Ventilation inhomogeneity in obstructive lung diseases measured by electrical impedance tomography: a simulation study,” *J. Clin. Monit. Comput.*, vol.32, no.4, pp.753-761, 2018.

[37] B. Schullcke, S. Krueger-Ziolek, B. Gong and K. Moeller, “A simulation study on the ventilation inhomogeneity measured with electrical impedance tomography,”*IFAC-PapersOnLine,*vol.50,no.1,pp.8781-8785,2017.

[38] Y. Lin and L. Huang, “Acoustic- and elastic-waveform inversion using a modified total-variation regularization scheme,” *Geophys. J. Int.*,vol.200,no.1,pp.489-502,2015.

[39] S. Osher, M. Burger, D. Goldfarb, J. Xu and W. Yin, ”An iterative regularization method for total variation-based image restoration,” *Multiscale Model. Simul.*,vol.4,no.2,pp.460-489,2005.

[40] M. Belge, M. Kilmer and E. L. Miller, "Simultaneous multiple regularizaiton parameter selection by means of the L-hypersurface with applications to linear inverse problems posed in the wavelet transform domain," *Proc. SPIE Int. Soc. Opt. Eng.*, vol. 3459, no. 1998, pp. 328-336, 1998.

[41] Z. Dou, B. Zhang and X. Yu, “A new alternating minimization algorithm for image segmentation,” *IETConf Publ*.,vol.2015,no. CP681,pp. 181-184,2015.

[42] N. Otsu, “A threshold selection method from gray-level histograms,”*IEEE Trans. Syst. ManCybern.*, vol. 9, no. 1, pp. 62-66, 1979.

[43] A. Vyas, M. B. Roopashree and B. R. Prasad, “Centroid detection by Gaussian pattern matching in adaptive optics,” *Int. J. Comput. Appli.*, vol. 1, no. 26, pp. 30-35, 2010.

[44] I. Frerichs, S. Pulletz, G. Elke, F. Reifferscheid, J. Scholz and N. Weiler, "Assessment of changes in distribution of lung perfusion by electrical impedance tomography", *Respiration*, vol. 77, no. 3, pp. 282-291, 2009.

[45] J. Riera, P. J. Riu. P. Casan and J. R. Masclans, "Electrical impedance tomography in acute lung injury", *Med. Intensiva*, vol. 35, no. 8, pp. 509-517, 2011.

[46] S. Leonhardt and B. Lachmann, "Electrical impedance tomography: the holy grail of ventilation and perfusion monitoring?", *Intensive Care Med.* , vol. 38, no. 12, pp. 1917-1929.